nature communications

Article

https://doi.org/10.1038/s41467-025-64749-5

Alignment of edge dislocations – the reason lying behind composition inhomogeneity induced low thermal conductivity

Received: 5 February 2025

Accepted: 24 September 2025

Published online: 05 November 2025

Check for updates

Siqi Liu[1,8], Wei-Di Liu[1,8] ✉, Wanyu Lyu[1,8], Liang-Cao Yin[2], Yicheng Yue[1], Han Gao[1,3], Meng Li[1], Xiao-Lei Shi[1], Qingfeng Liu[2], Ning Wang[4] ✉, James D. Riches[5], Dmitri V. Golberg[6,7] & Zhi-Gang Chen[1] ✉

Compositional inhomogeneity in a material can result in low thermal conductivity, benefiting applications such as thermoelectric energy conversion, energy gas storage, and thermal barrier coating. However, current understanding remains limited to effective thermal conductivity models, which largely overlook detailed structural features of the material. Here, taking $Bi_{0.4}Sb_{1.6}Te_3$ compound as a proof-of-concept material, we reveal that the true reason for low thermal conductivity determined by compositional inhomogeneity originates from randomly aligned edge dislocations. The random alignment of edge dislocations is consistent with the alignment of composition distribution. This is because these edge dislocations are primarily gathered at composition gradient domains between domains with different compositions, having preferential orientation along the composition gradient direction. This work offers a structural perspective on the mechanism underlying reduced thermal conductivity due to compositional inhomogeneity, providing valuable insights for designing materials with tailored thermal properties.

Low thermal conductivity (κ) is crucial for applications in thermal barrier coating[1,2], energy gas storage[3,4], and thermoelectric energy conversion[5–7], etc. Typically, reducing κ involves enhancing phonon and carrier scattering[8–11] through approaches like boundary engineering[12,13], porosity design[14,15], and composition tuning[16]. Among these, composition tuning is the most widely used[17,18], as it can be directly implemented by adjusting material content[19]. This strategy is generally understood in terms of point defects, assuming a homogeneous composition[20].

In addition to homogeneous compositions, inhomogeneous composition distribution is also commonly observed in low κ materials[21,22], affecting κ beyond the effects of point defects. Compositional inhomogeneity is typically analyzed by effective κ models[23–26], such as parallel model[27], series model[27], effective medium theory model[28], and Maxwell–Eucken model[29]. These models are based on the Fourier's Law[27–30], treating phases with varying volume fractions and the κ as individual components. However, this conventional approach neglects the impact of nanostructural features of the neighboring domains.

[1]School of Chemistry and Physics, ARC Research Hub in Zero-emission Power Generation for Carbon Neutrality, and Centre for Materials Science, Queensland University of Technology, Brisbane, QLD 4000, Australia. [2]State Key Laboratory of Materials-Oriented Chemical Engineering, College of Chemical Engineering, Nanjing Tech University, Nanjing 211816, China. [3]School of Physics, Zhengzhou University, Zhengzhou 450052, China. [4]College of Chemical Engineering, Qingdao University of Science and Technology, Qingdao 266042, China. [5]Central Analytical Research Facility (CARF), and Centre for Materials Science, Queensland University of Technology, Brisbane, QLD 4001, Australia. [6]School of Chemistry and Physics, and Centre for Materials Science, Queensland University of Technology, Brisbane, QLD 4000, Australia. [7]Research Centre for Materials Nanoarchitectonics (MANA), National Institute for Materials Science (NIMS), Tsukuba, Ibaraki 305, Japan. [8]These authors contributed equally: Siqi Liu, Wei-Di Liu, Wanyu Lyu. ✉e-mail: weidi.liu@qut.edu.au; 04031@qust.edu.cn; zhigang.chen@qut.edu.au

In this work, by taking $Bi_{0.4}Sb_{1.6}Te_3$ as a case study, we demonstrated that compositional inhomogeneity with randomly aligned edge dislocations enhances phonon scattering, leading to a lower κ. Compared to a directional composition distribution, a random composition distribution results in lower κ due to a higher density of randomly aligned edge dislocations. These dislocations arise from the lattice misfit due to composition gradient domains between Bi-rich and Sb-rich domains, featuring by a preferential orientation along the composition gradient direction (d_{CG}).

Results and discussion

Composition distribution influences thermal conductivity

To explore the relationship between compositional inhomogeneity and the κ in the as-prepared $Bi_{0.4}Sb_{1.6}Te_3$ pellet, scanning electron microscopy (SEM), energy-dispersive X-ray spectroscopy (EDS) and scanning thermal probe micro-image (STPM) measurements were performed on the same area from a well-polished flat surface, as shown in Fig. 1. The backscattered electron (BSE) image (Fig. 1a) reveals a scattered distribution of bright and dark areas, indicating the inhomogeneous composition[31]. The bright areas, identified as Bi-rich ones due to Bi higher atomic number, and the dark areas, Sb-rich with a lower atomic number, are corroborated by the EDS maps of Bi, Sb and Te (Fig. 1b, c and Supplementary Fig. 5).

Distinguished by the composition distribution pattern, only random composition distribution and directional composition distribution are detected. Bule and orange rectangular areas as shown in Fig. 1a are selected as representatives for random and directional composition gradient areas respectively. Notably, since our sample is prepared by melting method, which can be regarded as a quasi-steady-state process, the compositions of Bi-rich, composition gradient and Sb-rich domains, and the size of composition gradient domains (indicated by average width) can be considered consistent throughout the sample. As a result, magnitude difference between random and directional composition distribution areas are minimal. And the directional feature in composition gradient domains is more dominant than magnitude of variation. The STPM image (Fig. 1d) shows the κ distribution in the same area as in Fig. 1a. To ensure comparability of the result, the κ in random and directional composition distribution areas are measured along the same direction by same method under same condition in different areas. Areas with random composition distribution exhibit lower κ, this is attributed to randomly aligned edge dislocations that enhance phonon scattering (schematically shown in Fig. 1e). Conversely, areas with directional composition distribution display higher κ due to directionally aligned edge dislocations with relatively weaker phonon scattering (schematically shown in Fig. 1f). The correlation between composition distribution and κ difference is observed throughout the bulk sample, which is evidenced by SEM-EDS and

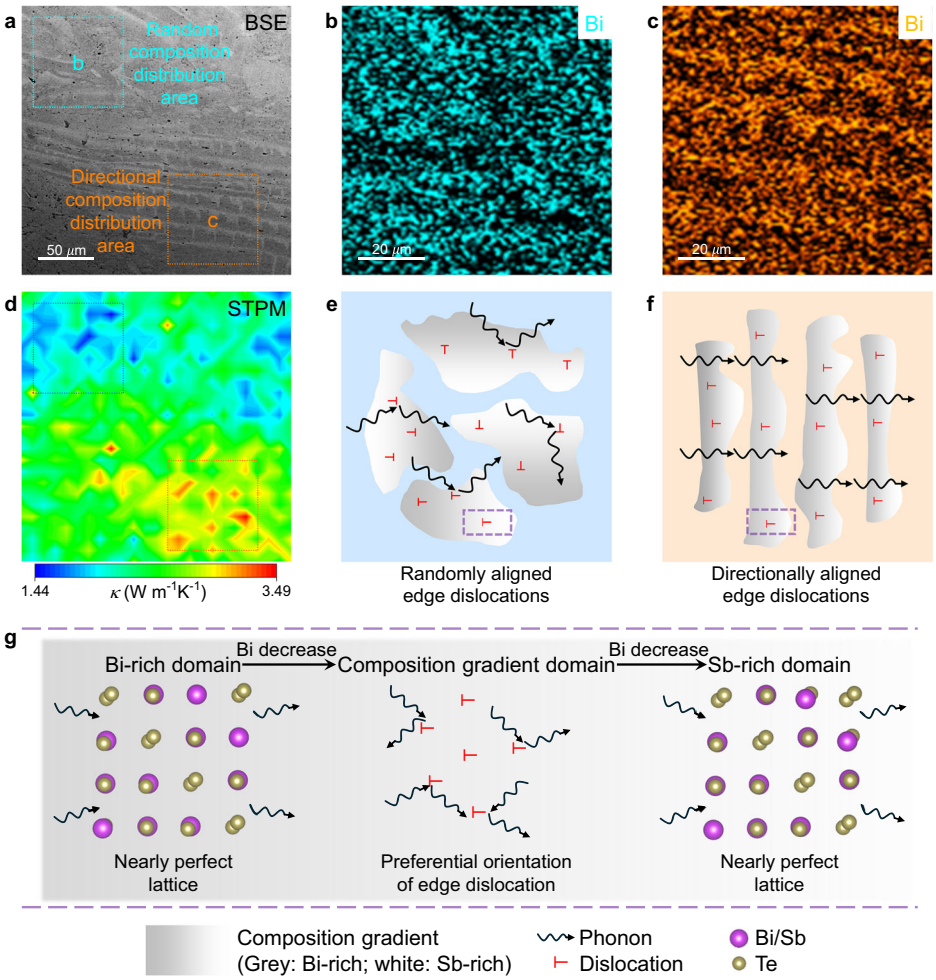

Fig. 1 | Influence of composition distribution on thermal conductivity. **a**, Backscattered electron (BSE) image showing the composition distribution of $Bi_{0.4}Sb_{1.6}Te_3$ pellet. Energy-dispersive X-ray spectroscopy (EDS) maps of Bi, illustrating areas with random (**b**) and uniform (**c**) composition distribution. **d** Scanning thermal probe micro-image (STPM) depicting the thermal conductivity (κ) distribution corresponding to the area in (**a**). Schematic illustrations on the influence of edge dislocations with different alignment types in areas exhibiting random (**e**) and directional composition distribution (**f**), respectively. **g** A schematic representation of the preferential orientation of edge dislocations along the composition gradient direction (d_{CG}).

STPM characterizations on areas at different depths, obtained by sequentially polishing off surface parts (Supplementary Figs. 6–8). Considering that composition inhomogeneity has minor influence on carrier concentration and corresponding electrical thermal conductivity[32], the low κ is mainly contributed by phonon transportation influenced by the random alignment of edge dislocations. This behavior is caused by preferential orientation of edge dislocations along the d_{CG}, as illustrated schematically in Fig. 1g. Notably, these edge dislocations are largely gathered at the composition gradient domains between Bi-rich and Sb-rich domains, being aligned with the macroscale composition gradient distribution. As shown in Supplementary Fig. 5, EDS quantitative analyses on random and directional composition distribution areas show similar compositions, indicating similar density of point defects in these areas. We have excluded the influence of density of point defect on κ from both thermodynamic and kinetic perspectives. From the thermodynamic perspective, composition is a dominant factor influencing the likelihood for point defect formation. According to EDS analysis shown in Supplementary Fig. 5, similar compositions have been observed in random composition distribution area ($Bi_{0.405}Sb_{1.645}Te_{2.95}$) and directional composition distribution area ($Bi_{0.405}Sb_{1.640}Te_{2.955}$), implying similar thermodynamic factors. From the kinetic perspective, synthesis conditions (e.g. sintering temperature[33], annealing temperature[34], cooling rate[35]) dominate the evolution of point defects. Since both random and directional composition distribution areas are observed in the same sample without special treatment in different areas, the synthesis conditions for them are the same (Supplementary Fig. 3). Therefore, the kinetic factors influencing point defect formation and corresponding density are also the same. Moreover, electron backscatter diffraction (EBSD) analysis is conducted on the same area of STPM measurement. As shown in Supplementary Fig. 9, crystallographic orientations of random and directional composition distribution areas are highly consistent, which can exclude the influence of texture on κ difference. Further details and implications of this alignment will be discussed in subsequent sections.

Composition gradient characterization

To investigate the composition and structure characteristics of the as-prepared $Bi_{0.4}Sb_{1.6}Te_3$ pellet, X-ray diffraction (XRD) and SEM-EDS analyses were performed (Fig. 2). The XRD pattern (Fig. 2a) matches well with the PDF#01-072-1836, with no additional peaks, confirming that sample solely consists of hexagonal $Bi_{0.4}Sb_{1.6}Te_3$ without any secondary phases.

Figure 2b compares the secondary electron (SE) and BSE images of the sample. While the SE image shows a flat surface without revealing grain boundaries, the BSE image of the same region reveals obvious contrast difference, indicating inhomogeneous composition where the bright areas have higher atomic number than the dark areas. To further analyze the composition distribution, Fig. 2c, d provide an enlarged BSE image of the area in Fig. 2b, along with the corresponding EDS maps and a line scan profile. These results confirm that the bright areas are Bi-rich, while the dark areas are Sb-rich. In contrast, Te is evenly distributed throughout the $Bi_{0.4}Sb_{1.6}Te_3$ pellet. As shown in Fig. 2d, the composition gradually changes from Sb-rich to Bi-rich and back to Bi-rich again. The domain with ~4.5 μm width between Bi-rich and Sb-rich domain is noted as composition gradient domain, which will be further characterized and discussed in subsequent sections. Notably, such composition distribution occurs throughout the sample rather than solely on the top surface as evidenced by additional EDS analysis from multiple perspectives (Supplementary Fig. 10). As shown in Supplementary Fig. 11c, the fracture SEM images indicate the average grain size is >80 μm, which is much larger than the as-selected area. Therefore, grain boundaries are not the reason for the κ difference in random and directional composition distribution areas. Also, according to the XRD and SEM-EDS analyses, the sample is solely composed of $Bi_{0.4}Sb_{1.6}Te_3$ without secondary phases, which can exclude the influence of secondary phase on the κ difference.

To quantitatively compare the composition between Bi-rich and Sb-rich domains, representative EDS point analyses were conducted, as shown in Fig. 2e (corresponding to points in Fig. 2c). The results reveal that the Bi-rich domain has significantly higher Bi content (10.9 at.%) compared to Sb-rich domains (6.7 at.%). Figure 2f provides a statistical summary of the average elemental content in Bi and Sb in Bi-rich and Sb-rich domains. On average, Bi-rich domains contain 10.4 at.% Bi, 30.1 at.% Sb, and 59.5 at.% Te, while Sb-rich domains contain 7.0 at.% Bi, 33.7 at.% Sb, and 59.3 at.% Te. This demonstrates the clear Bi and Sb composition differences in the neighboring areas, while Te content is similar in both areas.

Overall, Fig. 2 confirms the inhomogeneous Bi and Sb compositional distribution in the as-prepared $Bi_{0.4}Sb_{1.6}Te_3$ pellet without any secondary phases seen. The compositionally distinct areas are visually apparent, with Bi-rich domains appearing bright, and Sb-rich domains dark in the BSE images. Since both random and directional composition distribution areas contain widely distributed composition gradient domains, composition gradient domains are also not the reason for κ difference between random and directional composition distribution areas.

Lattice misfit and strain analysis

To examine the structural characteristics of the composition gradient domain between Bi-rich and Sb-rich domains, Fig. 3 presents the SE image of a focused ion beam (FIB) lamella cut off from the $Bi_{0.4}Sb_{1.6}Te_3$ pellet and corresponding transmission electron microscopy (TEM) analyses. Figure 3a provides an overview of the FIB lamella, spanning the Bi-rich and Sb-rich domains (cut-off location shown in Supplementary Fig. 12). A low-magnification TEM image (Fig. 3b) of the red rectangle area in Fig. 3a reveals a continuous, single grain structure without visible grain boundaries, nanoprecipitates or dislocation networks. Also, the almost even contrast throughout the whole sample reflects closely consistent thickness as shown in Fig. 3a, b. Figure 3c displays a Bi-content contour map of the same area, showing a decrease in Bi content from approximately 18.0 to 11.6 at.% from bottom left to top right. Notably, a composition gradient domain, approximately 4.5 μm wide, was observed between the Bi-rich and Sb-rich domains. These domains have been specified in Fig. 3b, c. Figure 3d–f presents high-resolution TEM (HRTEM) images and corresponding strain maps for the Bi-rich, composition gradient, and Sb-rich domains, respectively. Full strain maps with e_{xx}, e_{xy}, e_{yx} and e_{yy} for these areas are provided in Supplementary Fig. 13. Indicated by minor strain, the Bi-rich and Sb-rich domains exhibit nearly perfect lattice along the [10 5 $\bar{1}$] zone axes (indicated by selected area electron diffraction (SAED) patterns shown in Supplementary Fig. 14a and c). In contrast, the composition gradient domain (Fig. 3e) shows significantly larger lattice strain along the same zone axis (indicated by SAED patten shown in Supplementary Fig. 14b), compared with Bi-rich and Sb-rich domains.

To further analyze lattice structural features, planar distances of (0 1 5) planes ($d_{(0\ 1\ 5)}$) were examined in the Bi-rich, composition gradient, and Sb-rich domains (Fig. 3g–j). Enlarged HRTEM images (Fig. 3g–i) and typical line profiles (averaged over 10 consecutive planes) reveal $d_{(0\ 1\ 5)}$ values of 3.27 Å, 3.14 Å and 3.04 Å for the Bi-rich, composition gradient and Sb-rich domains, respectively. Figure 3j provides a statistical summary of $d_{(0\ 1\ 5)}$ measurements averaged over 10 selected areas in the Bi-rich, composition gradient, and Sb-rich domains (locations shown in Supplementary Fig. 15). There is a clear trend of decreasing $d_{(0\ 1\ 5)}$ with lowering Bi content from the Bi-rich domain through the composition gradient domain to the Sb-rich domain, driven by the difference in atomic radius between Bi (1.56 Å) and Sb (1.40 Å). Additionally, the composition gradient domain exhibits stronger fluctuations of $d_{(0\ 1\ 5)}$ (± 0.07 Å), compared to the Bi-rich

https://doi.org/10.1038/s41467-025-64749-5

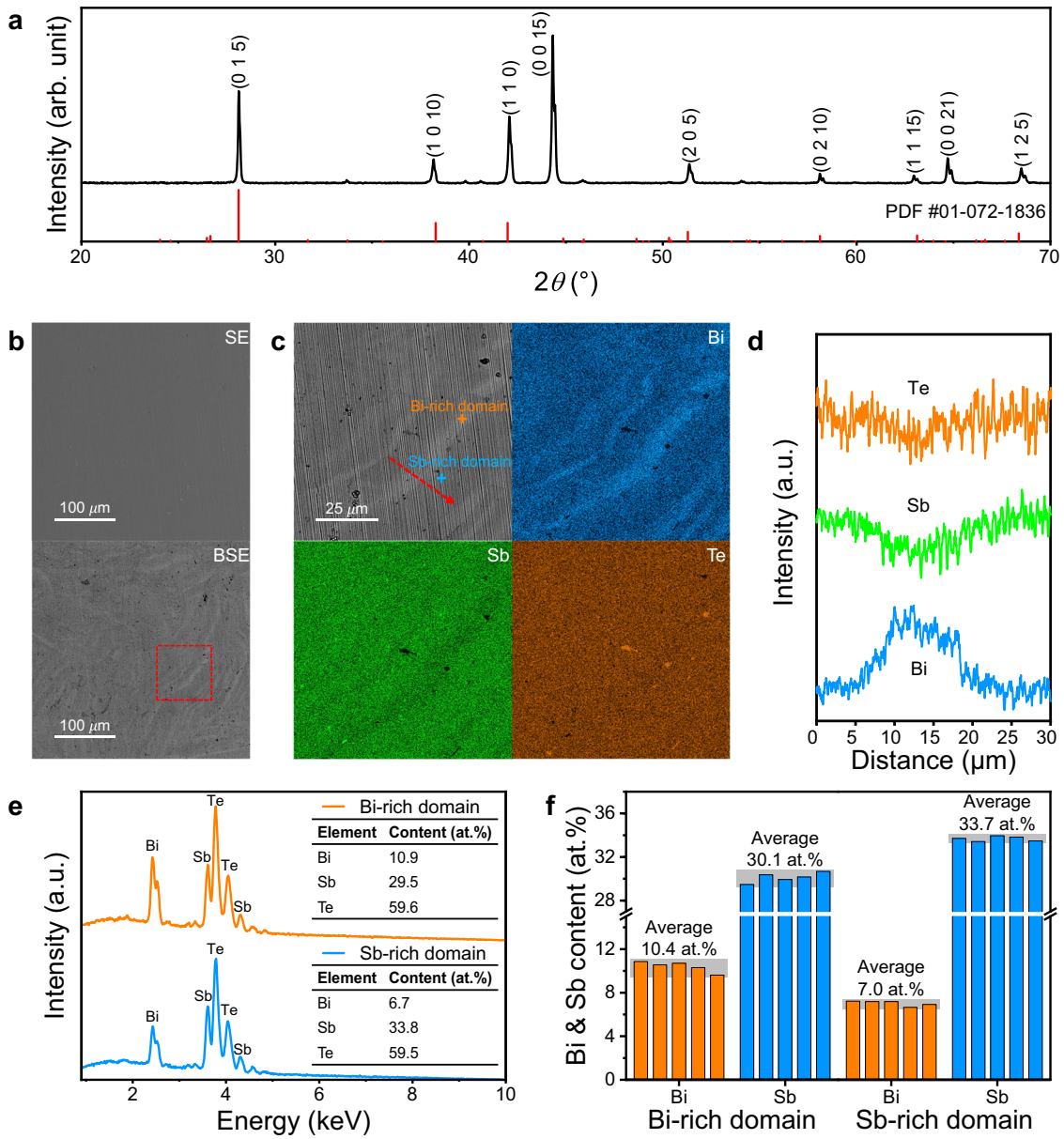

Fig. 2 | Structural and compositional characterization of the $Bi_{0.4}Sb_{1.6}Te_3$ pellet. a X-ray diffraction (XRD) pattern matching PDF #01-072-1836, confirming the absence of secondary phases. **b** Secondary electron (SE) and Backscattered electron (BSE) images highlighting compositional contrast, with Bi-rich domains appearing bright and Sb-rich domains dark. **c** BSE image of a selected region from (**b**) with corresponding energy-dispersive X-ray spectroscopy (EDS) maps for Bi, Sb, and Te distribution. **d** EDS line scan along the selected region in (**c**), showing compositional variation between Bi-rich and Sb-rich domains. **e** Representative EDS spectra from Bi-rich and Sb-rich domains in (**c**), with tables giving the elemental contents shown as insets. **f** Statistic summary of average atomic percentages of Bi and Sb in Bi-rich and Sb-rich domains.

(± 0.03 Å) and Sb-rich domains (± 0.03 Å), indicating denser lattice distortion. This is consistent with the denser lattice strain observed in the composition gradient domain.

Dislocation characterization and formation mechanism

To further elucidate the nanostructure characteristics of Bi-rich, composition gradient, and Sb-rich domains, additional HRTEM images and inverse fast Fourier transform (IFFT) images were analyzed, as shown in Fig. 4a–c. Edge dislocations are highlighted in the IFFT images. Both Bi-rich and Sb-rich domains exhibit nearly perfect lattice with a negligible amount of edge dislocations, whereas the composition gradient domain shows a significant accumulation of edge dislocations, indicative of a large lattice misfit. As shown in Fig. 4b, dislocations in composition gradient domain are highlighted. Based on the direction of extra half-planes (EHPs), dislocations with EHPs parallel to d_{CG} ($d_{EHPs} \parallel d_{CG}$) are highlighted in red and dislocations with EHPs perpendicular to d_{CG} ($d_{EHPs} \perp d_{CG}$) are highlighted in blue. As can be calculated, the overall dislocation density of the composition gradient domain is ~1.6×10^{12} cm^{-2}. Among them, ~77% are $d_{EHPs} \parallel d_{CG}$, the other ~23% are $d_{EHPs} \perp d_{CG}$. Such preferential orientation of edge dislocation along the d_{CG} can be attributed to the directional lattice distortion caused by the directional composition gradient, as illustrated in Fig. 4d. Considering dislocation density is concentrated in composition gradient domains, which widely exist in both random and directional composition distribution areas, dislocation density is also not the reason for the κ difference. Such preferential orientation of edge dislocation along the d_{CG} can be attributed to the directional lattice misfit caused by the directional composition distribution, as illustrated

https://doi.org/10.1038/s41467-025-64749-5

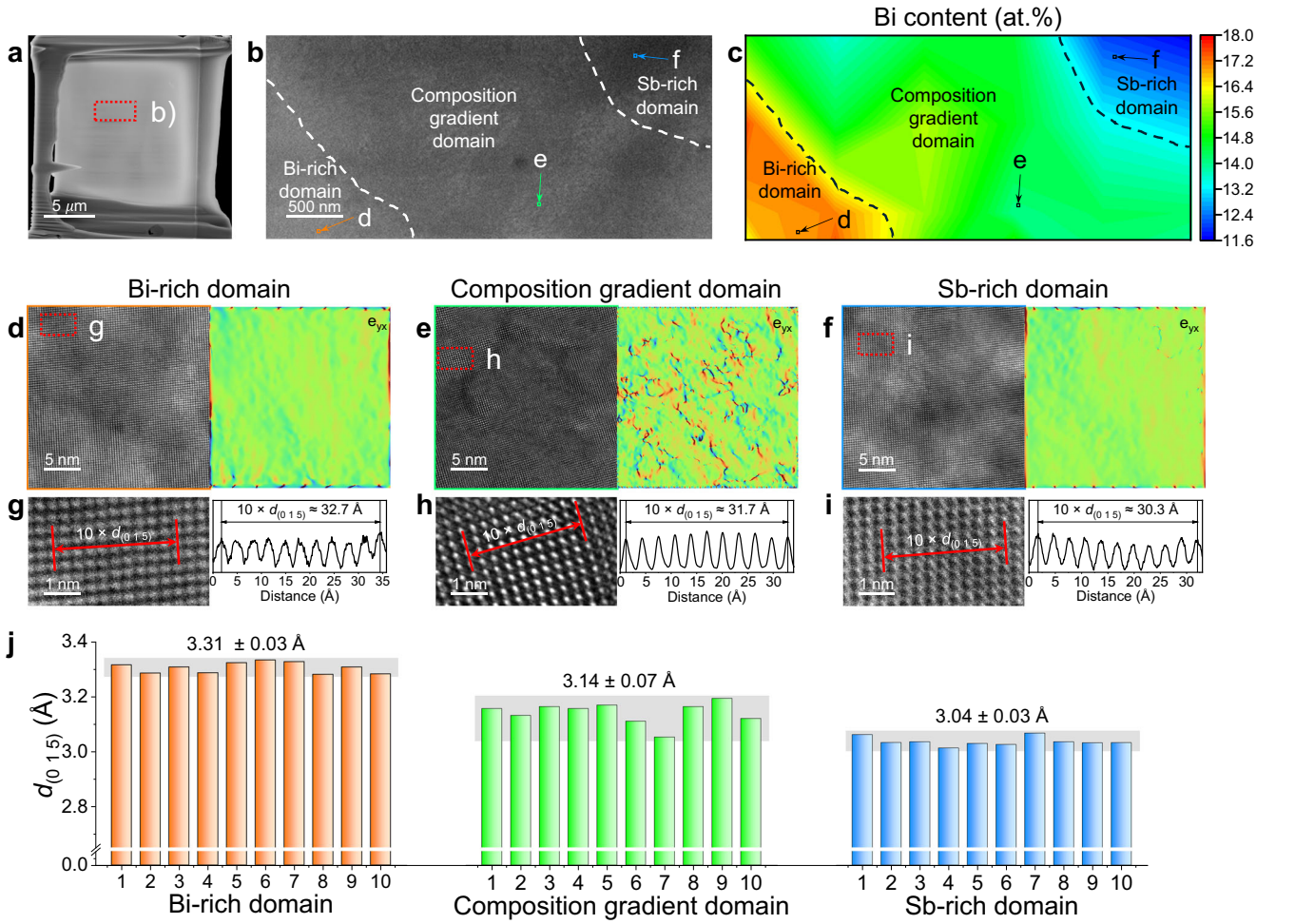

Fig. 3 | Analysis of lattice misfit and strain. a Secondary electron (SE) image of a focused ion beam (FIB) lamella cut off from the $Bi_{0.4}Sb_{1.6}Te_3$ pellet. **b** Low-magnification transmission electron microscopy (TEM) image of the selected area in (**a**), specifying Bi-rich, composition gradient and Sb-rich domains. **c** Contour map showing the distribution of Bi atomic content in the area shown in (**b**), specifying Bi-rich, composition gradient and Sb-rich domains. High-resolution TEM (HRTEM) images and strain maps of Bi-rich (**d**), composition gradient (**e**), and Sb-rich (**f**) domains, respectively, corresponding to the highlighted areas in (**b**) and (**c**). Enlarged HRTEM images and corresponding line profiles of selected areas in Bi-rich (**g**), composition gradient (**h**), and Sb-rich (**i**) domains, respectively. **j** Statistical comparison of planar distances of (0 1 5) plane ($d_{(0\,1\,5)}$) among Bi-rich, composition gradient, and Sb-rich domains.

in Fig. 4d. To support this observation, density functional theory (DFT) calculations were conducted to evaluate the formation energy of edge dislocations (EDF) under different conditions. As shown in Fig. 4e, the $E_{DF,\parallel}$ ($d_{EHPs} \parallel d_{CG}$) is much lower than $E_{DF,\perp}$ ($d_{EHPs} \perp d_{CG}$), which accounts for the preferential orientation of edge dislocations along the d_{CG}. Notably, when applying electron sectioning method on composition gradient domain[36], high-resolution scanning transmission electron microscopy (HRSTEM) images with focal planes at different depths indicate that no screw dislocation is observed in the composition gradient domain (Supplementary Fig. 16). Therefore, screw dislocations or mixed-type dislocations are not the reason for the κ difference in random and directional composition distribution areas.

In conclusion, as exemplified by a $Bi_{0.4}Sb_{1.6}Te_3$ compound, we identified the mechanism of low κ in materials with an inhomogeneous composition distribution. This can be explained by the randomly aligned edge dislocations at the composition gradient domains, between domains with different compositions. At the microscale, Bi-rich and Sb-rich domains exhibit nearly defect-free structures. However, in the composition gradient domain between Bi-rich and Sb-rich domains, a significant atomic radius difference between Bi and Sb results in a large lattice misfit. This misfit leads to the formation of a dense array of edge dislocations, which preferentially align along the composition gradient direction (d_{CG}) due to a lower edge dislocation formation energy parallel to this orientation ($E_{DF,\parallel}$) compared to that perpendicular to it ($E_{DF,\perp}$). At the macroscale, random composition distribution can lead to randomly aligned edge dislocations, contributing to strengthened phonon scattering, and lower κ compared to areas with directional composition distribution. In our discussion, influences of nanostructures, point defects, screw dislocation, dislocation density, composition gradient domains, grain boundaries or phase boundaries have all been well excluded. Therefore, low κ in random composition distribution area should be dominated by the random alignment of edge dislocations induced by random alignment of composition gradients. This insight reveals the origin of low κ in compositional inhomogeneous materials from the microstructure viewpoint, which can provide valuable guidance for the design of future materials with optimized thermal properties.

Methods

Synthesis and characterization

Polycrystalline $Bi_{0.4}Sb_{1.6}Te_3$ samples were synthesized by melting stoichiometric ratios of Bi, Sb, Te (99.99%, Chengdu optoelectronic materials Co., Ltd.) in evacuated and carbon-coated silica tubes. The mixtures were heated up to 773 K at 2 K min^{-1}, held for 2 h, then further heated to 1223 K at 1 K min^{-1}, maintained for 5 h, and quenched in ice water. The acquired ingots were ground into powder using an agate

https://doi.org/10.1038/s41467-025-64749-5

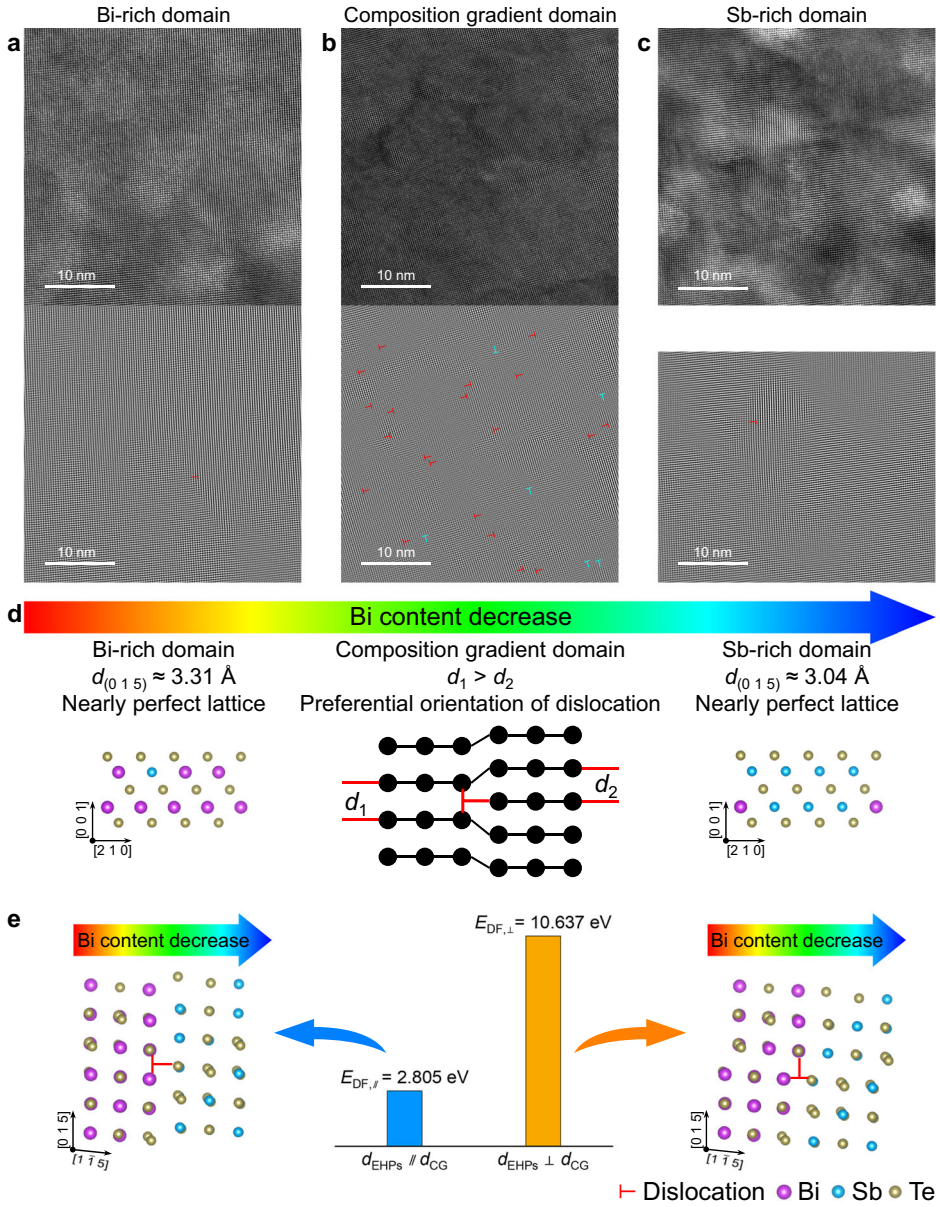

Fig. 4 | Edge dislocation characterization and analysis. High-resolution TEM (HRTEM) images and corresponding inverse fast Fourier transform (IFFT) images of Bi-rich (**a**), composition gradient (**b**), and Sb-rich (**c**) domains. **d** Schematic diagram illustrating the preferential orientation of edge dislocations along with composition gradient direction. **e** Density functional theory (DFT) calculated edge dislocation formation energy (EDF) for extra half-planes (EHPs) grown along and perpendicular to composition gradient direction (d_{CG}), respectively.

mortar and sieved through a 50-mesh screen. The powders were consolidated by spark plasma sintering (SPS; LABOX-110H, Sinter Land, Japan) at 723 K under 50 MPa in a Ø12.7 mm graphite mold for 5 min. (Supplementary Fig. 3)

The phase composition of samples was inspected by X-ray diffraction (XRD) (SmartLab, Cu Kα line, Rigaku, Japan). The κ distribution was measured by calibrated Scanning Thermal Probe Micro-image (STPM-1000 Advance Riko, Japan). After calibration, thermal conductivities of standard materials are verified by Laser Flash Analysis (LFA 467 Hyperflash, Netzsch, German). Secondary electrons (SE) and backscatter electrons (BSE) images were taken by field emission scanning electron microscopy (FESEM) (SU7000, Hitachi, Japan) with energy-dispersive X-ray spectroscopy (EDS) (Ultim Max 100, Oxford, British) and field-free Ultra-High Resolution (UHR) FESEM (S8000X, TESCAN, Czech Republic). The characterization of the sample's atomic structure was carried out using high-resolution transmission electron microscopy (HRTEM) (JEM-2100 and JEM-ARM200F, JEOL, Japan). The samples for TEM observations were prepared by focused ion beam (FIB) milling (S8000X, TESCAN, Czech Republic).

DFT calculations

DFT calculations were performed using a projector-augmented wave (PAW) method implemented in the Vienna Ab initio Simulation Package (VASP). The fully relativistic Perdew–Burke–Ernzerh generalized gradient approximation functional (GGA-PBE) was employed to model exchange correlation interactions. A fundamental supercell comprising of 90 atoms without edge dislocation was constructed by cleaving six atomic layers in (0 1 5) planes from a $3 \times 3 \times 3$ $Bi_{0.4}Sb_{1.6}Te_3$ supercell, followed by the addition of a 15 Å vacuum slab[37]. Supercells with edge dislocation parallel and perpendicular to the composition gradient direction were constructed by slipping the (0 1 5) and (1 $\bar{1}$ 5) planes by 50% of planar distance along respective directions[38]. The supercell

energy was calculated with a plane wave cut-off energy of 400 eV, based on which the dislocation formation energy of the two configurations were further evaluated.

STPM analysis

The STPM measures the Seebeck coefficient and thermal properties distribution at the sample surface by using a thermal probe and measuring the voltage and temperature of the probe. As can be seen in Supplementary Fig. 1, STPM measures κ along the out-of-plane direction as the temperature gradient is applied perpendicular to the sample surface. The spatial resolution of the equipment is 20 μm. In order to improve the accuracy of STPM, 7 standard materials (Si, Ta, Ge, SUS304, $SrTiO_3$, SiO_2 glass and Vespel) are used to calibrate the equipment before sample measurement. After calibration, the κ of each standard materials are verified by Laser Flash Analysis (LFA). As a result, the accuracy of STPM can reach ~13%. More detailed discussions are available in Supplementary Note 1.

Data availability

The data generated in this study is provided in the Source Data file. Source data are provided with this paper.

References

1. Klemens, P. G. & Gell, M. Thermal Conductivity of Thermal barrier coatings. *Mater. Sci. Eng. A-Struct. Mater. Prop. Microstruct. Process.* **245**, 143–149 (1998).
2. Jackson, R. W. et al. Interaction of molten silicates with thermal barrier coatings under temperature gradients. *Acta Mater.* **89**, 396–407 (2015).
3. Babaei, H. et al. Observation of reduced thermal conductivity in a metal-organic framework due to the presence of adsorbates. *Nat. Commun.* **11**, 8 (2020).
4. Wieme, J. et al. Thermal Engineering of Metal-Organic Frameworks for Adsorption Applications: A Molecular Simulation Perspective. *ACS Appl. Mater. Interfaces* **11**, 38697–38707 (2019).
5. Qin, B. C. et al. Power generation and thermoelectric cooling enabled by momentum and energy multiband alignments. *Science* **373**, 556–561 (2021).
6. Wang, D. Z. et al. Decoupling Carrier-Phonon Scattering Boosts the Thermoelectric Performance of n-Type GeTe-Based Materials. *J. Am. Chem. Soc.* **146**, 1681–1689 (2024).
7. Liu, W. D. et al. Grain boundary re-crystallization and sub-nano regions leading to high plateau figure of merit for Bi_2Te_3 nanoflakes. *Energy Environ. Sci.* **16**, 5123–5135 (2023).
8. Yang, G. S. et al. Enhanced thermoelectric performance and mechanical strength of n-type BiTeSe materials produced via a composite strategy. *Chem. Eng. J.* **428**, 9 (2022).
9. Yan, Q. Y. & Kanatzidis, M. G. High-performance thermoelectrics and challenges for practical devices. *Nat. Mater.* **21**, 503–513 (2022).
10. Wang, D. Y. et al. Multi-heterojunctioned plastics with high thermoelectric figure of merit. *Nature* **632**, 11 (2024).
11. Jiang, Y. L. et al. Exceptional figure of merit achieved in boron-dispersed GeTe-based thermoelectric composites. *Nat. Commun.* **15**, 10 (2024).
12. Dong, H. C., Wen, B. & Melnik, R. Relative importance of grain boundaries and size effects in thermal conductivity of nanocrystalline materials. *Sci. Rep.* **4**, 5 (2014).
13. Fujii, S., Yokoi, T., Fisher, C. A. J., Moriwake, H. & Yoshiya, M. Quantitative prediction of grain boundary thermal conductivities from local atomic environments. *Nat. Commun.* **11**, 10 (2020).
14. Liu, H. & Zhao, X. P. Thermal Conductivity Analysis of High Porosity Structures with Open and Closed Pores. *Int. J. Heat. Mass Transf.* **183**, 11 (2022).
15. Stallard, S., Jiang, H., Chen, Y. Y., Bergman, T. L. & Li, X. L. Exploring the design space of the effective thermal conductivity, permeability, and stiffness of high-porosity foams. *Mater. Des.* **231**, 10 (2023).
16. Burlayenko, V. N., Altenbach, H., Sadowski, T., Dimitrova, S. D. & Bhaskar, A. Modelling functionally graded materials in heat transfer and thermal stress analysis by means of graded finite elements. *Appl. Math. Model.* **45**, 422–438 (2017).
17. Jung, Y. et al. Thermal Transport Properties of Phonons in Halide Perovskites. *Adv. Mater.* **35**, 28 (2023).
18. Wang, G. et al. Tuning Thermal Conductivity of Hybrid Perovskites through Halide Alloying. *Adv. Sci.* **11**, 9 (2024).
19. Chen, G. J. et al. A novel approach for the composition design of high-entropy fluorite oxides with low thermal conductivity. *J. Adv. Ceram.* **13**, 1369–1381 (2024).
20. Shi, T. et al. Spatial inhomogeneity of point defect properties in refractory multi-principal element alloy with short-range order: A first-principles study. *J. Appl. Phys.* **133**, 075103 (2023).
21. Zhao, M. et al. Defect engineering in development of low thermal conductivity materials: A review. *J. Eur. Ceram. Soc.* **37**, 1–13 (2017).
22. Lee, W. et al. Effect of inhomogeneous composition on the thermal conductivity of an Al alloy during the precipitation-hardening process. *J. Mater. Res. Technol.-JMRT* **9**, 9 (2020).
23. Cheng, S. C. & Vachon, R. I. Prediction of Thermal Conductivity of 2-Phase and 3-Phase Solid Heterogeneous Mixtures. *Int. J. Heat. Mass Transf.* **12**, 249–264 (1969).
24. Progelhof, R. C., Throne, J. L. & Ruetsch, R. R. Methods for Predicting Thermal Conductivity of Composite Systems. *Polym. Eng. Sci.* **16**, 615–625 (1976).
25. Carson, J. K., Lovatt, S. J., Tanner, D. J. & Cleland, A. C. An analysis of the influence of material structure on the effective thermal conductivity of theoretical porous materials using finite element simulations. *Int. J. Refrig. -Rev. Int. Froid* **26**, 8 (2003).
26. Floury, J., Carson, J. & Pham, Q. T. Modelling Thermal Conductivity in Heterogeneous Media with the Finite Element Method. *Food Bioprocess Technol.* **1**, 10 (2008).
27. Chu, Z. X., Zhou, G. Q., Wang, Y. J., Mo, P. Q. & Tang, R. Thermal-physical properties of selected geomaterials: coal, sandstone and concrete based on basic series and parallel models. *Environ. Earth Sci.* **77**, 19 (2018).
28. Davis, H. T., Valencourt, L. R. & Johnson, C. E. Transport Processes in Composite Media. *J. Am. Ceram. Soc.* **58**, 446–452 (1975).
29. Eucken, A. Allgemeine Gesetzmäßigkeiten für das Wärmeleitvermögen verschiedener Stoffarten und Aggregatzustände. *Forsch. Auf Dem Geb. des. Ingenieurwesens A* **11**, 6–20 (1940).
30. Noh, H. G., Kang, H. C., Kim, M. H. & Park, H. S. Estimation Model for Effective Thermal Conductivity of Reinforced Concrete Containing Multiple Round Rebars. *Int. J. Concr. Struct. Mater.* **12**, 10 (2018).
31. Liu, C. H., Wu, H. J. & Chen, S. W. Liquidus Projection of the Ternary Bi-Sb-Te Thermoelectric Material System. *Metall. Mater. Trans. A* **44A**, 10 (2013).
32. Zheng, Y. et al. Mechanically Robust BiSbTe Alloys with Superior Thermoelectric Performance: A Case Study of Stable Hierarchical Nanostructured Thermoelectric Materials. *Adv. Energy Mater.* **5**, 11 (2015).
33. Zhang, Q. et al. Evolution of the Intrinsic Point Defects in Bismuth Telluride-Based Thermoelectric Materials. *ACS Appl. Mater. Interfaces* **11**, 41424–41431 (2019).
34. Kianwimol, S., Sakdanuphab, R., Chanlek, N., Harnwunggmoung, A. & Sakulkalavek, A. Effect of annealing temperature on thermoelectric properties of bismuth telluride thick film deposited by DC magnetron sputtering. *Surf. Coat. Technol.* **393**, 8 (2020).
35. Wang, S. Y., Xie, W. J., Li, H., Tang, X. F. & Zhang, Q. J. Effects of Cooling Rate on Thermoelectric Properties of n-Type

$Bi_2(Se_{0.4}Te_{0.6})_3$ Compounds. *J. Electron. Mater.* **40**, 1150–1157 (2011).
36. Yang, H. et al. Imaging screw dislocations at atomic resolution by aberration-corrected electron optical sectioning. *Nat. Commun.* **6**, 7 (2015).
37. Momma, K. & Izumi, F. *VESTA 3* for three-dimensional visualization of crystal, volumetric and morphology data. *J. Appl. Crystallogr.* **44**, 1272–1276 (2011).
38. Lazewski, J. et al. DFT modelling of the edge dislocation in 4H-SiC. *J. Mater. Sci.* **54**, 10737–10745 (2019).

Acknowledgements

This work was financially supported by the Australian Research Council, HBIS-UQ Innovation Centre for Sustainable Steel project, and QUT Capacity Building Professor Program. The calculations were carried out in the National Computational Infrastructure, supported by the Australian government, for providing computational resources and service. The authors acknowledge Queensland Cyber Infrastructure Foundation Ltd (Project pe62) for providing computation allocation. This work was enabled using the Central Analytical Research Facility hosted at QUT.

Author contributions

Siqi Liu: Conceptualization, Methodology, Writing Original Draft. Wei-Di Liu: Conceptualization, Writing, Reviewing and Editing, Computation, Funding acquisition, Supervision. Wanyu Lyu: Methodology. Liang-Cao Yin: Methodology. Yicheng Yue: Methodology. Han Gao: Validation. Meng Li: Validation. Xiao-Lei Shi: Validation. Qingfeng Liu: Validation. Ning Wang: Validation. James D. Riches: Validation. Dmitri V. Golberg: Writing, Reviewing and Editing, Supervision. Zhi-Gang Chen: Writing, Reviewing and Editing, Funding acquisition, Supervision.

Competing interests

The authors declare no competing interests.

Additional information

Supplementary information The online version contains supplementary material available at https://doi.org/10.1038/s41467-025-64749-5.

Correspondence and requests for materials should be addressed to Wei-Di Liu, Ning Wang or Zhi-Gang Chen.

Peer review information *Nature Communications* thanks Yung-Kang Kuo and the other anonymous reviewer(s) for their contribution to the peer review of this work. A peer review file is available.

Terms and Conditions

Springer Nature journal content, brought to you courtesy of Springer Nature Customer Service Center GmbH (“Springer Nature”).
Springer Nature supports a reasonable amount of sharing of research papers by authors, subscribers and authorised users (“Users”), for small-scale personal, non-commercial use provided that all copyright, trade and service marks and other proprietary notices are maintained. By accessing, sharing, receiving or otherwise using the Springer Nature journal content you agree to these terms of use (“Terms”). For these purposes, Springer Nature considers academic use (by researchers and students) to be non-commercial.
These Terms are supplementary and will apply in addition to any applicable website terms and conditions, a relevant site licence or a personal subscription. These Terms will prevail over any conflict or ambiguity with regards to the relevant terms, a site licence or a personal subscription (to the extent of the conflict or ambiguity only). For Creative Commons-licensed articles, the terms of the Creative Commons license used will apply.
We collect and use personal data to provide access to the Springer Nature journal content. We may also use these personal data internally within ResearchGate and Springer Nature and as agreed share it, in an anonymised way, for purposes of tracking, analysis and reporting. We will not otherwise disclose your personal data outside the ResearchGate or the Springer Nature group of companies unless we have your permission as detailed in the Privacy Policy.
While Users may use the Springer Nature journal content for small scale, personal non-commercial use, it is important to note that Users may not:

1. use such content for the purpose of providing other users with access on a regular or large scale basis or as a means to circumvent access control;
2. use such content where to do so would be considered a criminal or statutory offence in any jurisdiction, or gives rise to civil liability, or is otherwise unlawful;
3. falsely or misleadingly imply or suggest endorsement, approval , sponsorship, or association unless explicitly agreed to by Springer Nature in writing;
4. use bots or other automated methods to access the content or redirect messages
5. override any security feature or exclusionary protocol; or
6. share the content in order to create substitute for Springer Nature products or services or a systematic database of Springer Nature journal content.

In line with the restriction against commercial use, Springer Nature does not permit the creation of a product or service that creates revenue, royalties, rent or income from our content or its inclusion as part of a paid for service or for other commercial gain. Springer Nature journal content cannot be used for inter-library loans and librarians may not upload Springer Nature journal content on a large scale into their, or any other, institutional repository.
These terms of use are reviewed regularly and may be amended at any time. Springer Nature is not obligated to publish any information or content on this website and may remove it or features or functionality at our sole discretion, at any time with or without notice. Springer Nature may revoke this licence to you at any time and remove access to any copies of the Springer Nature journal content which have been saved.
To the fullest extent permitted by law, Springer Nature makes no warranties, representations or guarantees to Users, either express or implied with respect to the Springer nature journal content and all parties disclaim and waive any implied warranties or warranties imposed by law, including merchantability or fitness for any particular purpose.
Please note that these rights do not automatically extend to content, data or other material published by Springer Nature that may be licensed from third parties.
If you would like to use or distribute our Springer Nature journal content to a wider audience or on a regular basis or in any other manner not expressly permitted by these Terms, please contact Springer Nature at

onlineservice@springernature.com